Front. Phys., 2012, 7(2): 175–192
DOI 10.1007/s11467-011-0197-9

REVIEW ARTICLE

# Studies on the electronic structures of three-dimensional topological insulators by angle resolved photoemission spectroscopy

**Yulin Chen**[1,2,3]

[1] *Department of Physics, University of Oxford, Clarendon Laboratory, Parks Road, Oxford, OX1 3PU, UK*
[2] *Stanford Institute for Materials and Energy Sciences, SLAC National Accelerator Laboratory, 2575 Sand Hill Road, Menlo Park, CA 94025, USA*
[3] *Geballe Laboratory for Advanced Materials, Departments of Physics and Applied Physics, Stanford University, Stanford, CA 94305, USA*
*E-mail: Yulin.Chen@physics.ox.ac.uk*
*Received June 7, 2011; accepted July 8, 2011*

Three-dimensional (3D) topological insulators represent a new state of quantum matter with a bulk gap and odd number of relativistic Dirac fermions on the surface. The unusual surface states of topological insulators rise from the nontrivial topology of their electronic structures as a result of strong spin–orbital coupling. In this review, we will briefly introduce the concept of topological insulators and the experimental method that can directly probe their unique electronic structure: angle resolved photoemission spectroscopy (ARPES). A few examples are then presented to demonstrate the unique band structures of different families of topological insulators and the unusual properties of the topological surface states. Finally, we will briefly discuss the future development of topological quantum materials.

**Keywords** topological insulator (TI), photoemission, ARPES

**PACS numbers** 71.18.+y, 71.20.-b, 73.20.-r, 73.23.-b

Contents

1 Introduction to topological insulators 175
2 Angle resolved photoemission spectroscopy 177
2.1 Basic concept 177
2.2 General principle 178
2.3 Experimental setup for angle resolved photoemission spectroscopy 179
3 Electronic structure of 3D topological insulators (TIs) 181
3.1 $Bi_xSb_{1-x}$ alloy 181
3.2 Single Dirac cone TIs from $V_2$–$VI_3$ compounds 182
3.3 Effects of non-magnetic and magnetic impurities 184
3.4 Search for other TI materials 187
3.5 Other topological states and perspectives 190
Acknowledgements 190
References 191

## 1 Introduction to topological insulators

In condensed matter physics, one of the central topics is to study why a handful of elements on earth can make up of thousands and thousands of substances with vastly different properties. To work on such a large quantity of materials, classification of them is thus of great importance. Until recently, different states of matter are usually classified by the spontaneous breaking of symmetries [1]. As examples, a crystal breaks translation symmetry; a magnet breaks rotation symmetry; a superconductor breaks the more subtle gauge symmetry.

The deficiency of this classification was first realized in 1980, when the quantum Hall (QH) state, a new state of matter that does not have spontaneous broken symmetry was discovered [2]. In this state, the bulk of the two-dimensional (2D) material is insulating, while the dissipationless chiral electric current can flow only along the sample edge, giving rise to a quantized Hall effect. The topological nature of the QH state soon came to light [3, 4] and a topological invariant, the first Chern number defined by the global properties of all occupied Bloch states of the materials can be used to characterize the state, making the QH state topologically distinct from all previously known states of matter.

©Higher Education Press and Springer-Verlag Berlin Heidelberg 2012

Recently, a new class of topological state, $Z_2$ topological insulators (TIs), have emerged. TIs represent a novel quantum matter with a bulk gap and odd number of relativistic Dirac fermions on the surface [5–7]. Similar to the QH state, this state can also be characterized by a topological invariant, $Z_2$ number [6–8]; but different from the QH state where the Chern number characterizing the topological order can have any integer values, the $Z_2$ number of TIs can possess only two values: 0 or 1. The value 0 indicates that the material's electronic structure is similar to a "normal" insulator, which is topologically equivalent to vacuum; and the value 1 indicates that the material is topologically non-trivial, forming a new state topologically distinct from all other known states of matter, including the QH state.

The prediction of this new state of quantum matter immediately inspired intensive studies in the field of condensed matter physics [5–28] including both theoretical and experimental efforts.

The 2D TI state, or the quantum spin Hall (QSH) state, was first investigated based on graphene [9]. However, it was soon realized that the spin-orbital coupling in graphene was too small to make the experimental observations feasible [29, 30]. Before long, a more realistic material system was proposed in the HgTe quantum well [10]. Shortly after the theoretical prediction [10], the QSH state was observed by electric transport experiments in the HgTe quantum well [11]. In the thick HgTe quantum well where the QSH state exist, there is an insulating gap in the bulk and gapless states at the edge where electrons with opposite spins counter-propagate [Fig. 1(a)], forming a single massless Dirac fermion at the edge [Fig. 1(b)]. The crossing of their dispersion branches at a time reversal invariant point (Dirac point) is protected by the time reversal symmetry (TRS) [6–8].

Soon the TI state was generalized to three-dimension (3D) [7, 18, 21, 22]. In a 3D TI, there exists an insulating bulk energy gap, but electrons can flow on its 2D surface [Fig. 1(c)], with their spin polarization locked to the momentum [Fig. 1(c)], forming a cone-shape dispersion with helical spin structure [Dirac cone, see Fig. 1(d)]. The spin degenerate points of these Dirac cones (Dirac points) reside at the time reversal invariant points in $k$-space [7, 18, 21, 22]. Up to date, several families of 3D TIs including tens of materials have been theoretically predicted, such as the $Bi_{1-x}Sb_x$ alloy ($x = 0.07 \sim 0.22$) [6]; $V_2$–$VI_3$ binary compounds ($Bi_2Te_3$, $Bi_2Se_3$ and $Sb_2Te_3$) [13], Ⅲ–V–$VI_2$ ternary compounds ($TlBiSe_2$) [27, 31] and many Heusler alloys [32, 33]. Experimental efforts soon followed and proved many of the predictions.

Unlike in the 2D QSH state, where the edge current flows strictly dissipationless and make the electric transport experiments most effective in determining its topological nature [11], the transport measurements can hardly determine the 3D TI materials. It is not only because the contribution from the surface state is smaller in the conductivity and it is hard to distinguish the bulk and surface contributions; but also because the 2D surface state of 3D TIs does not lead to complete suppression of electric resistance as in the 2D QSH states due to small angle scatterings [7]. Thus an experimental method is needed which can measure the electronic structure and directly separate the bulk and surface contributions.

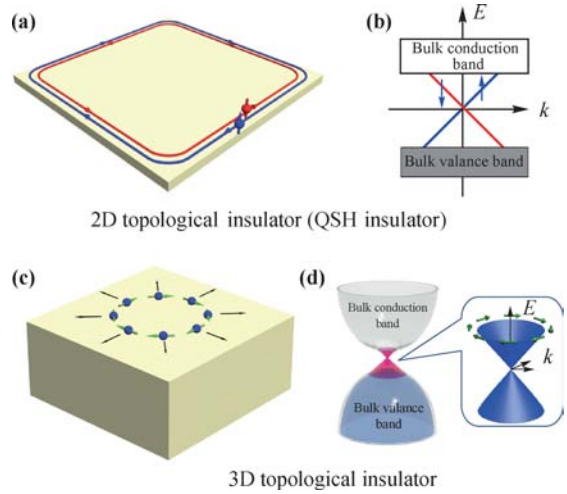


**Fig. 1** **(a)** Illustration of the spin-dependent electric currents flow around the edge of a 2D TI in real space. **(b)** $k$-space dispersion of the two branches of linearly dispersed edge state bands shown in (a). **(c)** Correlation between the surface state electron moment and spin polarization of a 3D TI. **(d)** Band diagram of a 3D TI in $k$-space, featuring a bulk band gap and an in-gap Dirac cone formed by the 2D surface state.

With these requirements, angle-resolved photoemission spectroscopy (ARPES) stands as a natural choice due to its capability of directly observing electronic band structure in solids. Because of the suitable mean free path of photoelectrons (1∼ 10 nm), the ARPES signal comes primarily from the top most unit-cells of the materials (Fig. 2), thus making the surface state contribution prominent in the total spectra. In addition, by

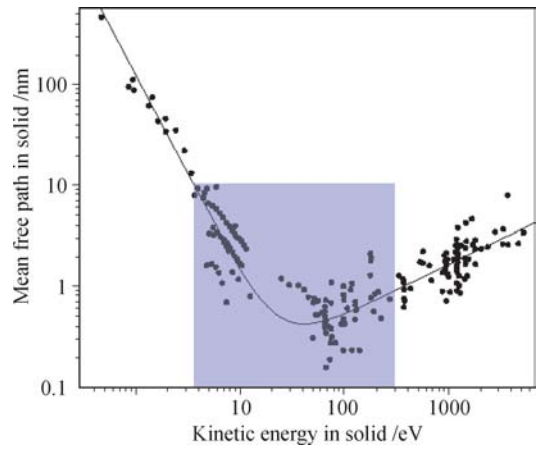


**Fig. 2** The "universal curve" for surface sensitivity in photoemission. Electron elastic mean free paths from various materials are plotted versus their kinetic energy in the solid. For regular ARPES measurements ($E_k$ range from a few to a few hundred eVs), mean free path range from 0.1 to 10 nms. Reproduced from Ref. [34]. Copyright © 1979 John Wiley & Sons, Inc.

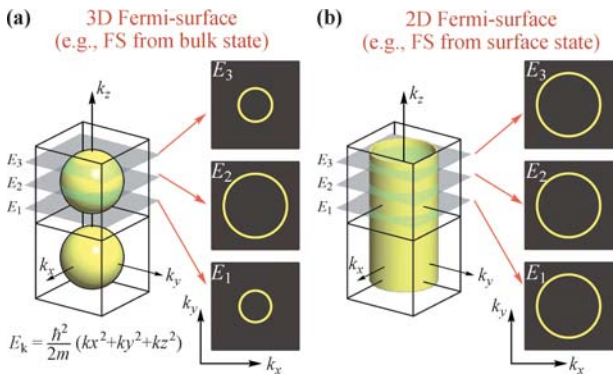


**Fig. 3** Illustration of the different photon-energy dependent ARPES result for 3D and 2D Fermi-surfaces (FSs). **(a)** Different FSs measured by ARPES under different photon energies due to the $k_z$ dispersion in $k$-space of a 3D FS. **(b)** Photon-energy dependent ARPES on a 2D FS results in identical FSs due to the absence of the $k_z$ dispersion.

performing photon-energy dependent measurements (Fig. 3), ARPES can easily separate the bulk and surface band structures because of their different $k_z$ dispersions. These advantages, together with its in plane $k$-space resolution, overcome the disadvantages encountered in the transport measurements as discussed above, making ARPES the most important method for studying the unique electronic structure of 3D TIs [12, 14–16, 25]. Furthermore, the ability of coupling the spin-detector to ARPES spectrometer makes it suitable to study the non-trivial helical spin-structure of TIs.

In the following sections, we will first briefly review this powerful experimental tool, and then present a few examples of the application of ARPES on 3D TIs.

## 2 Angle resolved photoemission spectroscopy

### 2.1 Basic concept

Angle resolved photoemission spectroscopy is a direct experimental technique to observe the distribution of electrons in solid, or more precisely, the density of single particle electronic excitations in the reciprocal (momentum, or $k$-) space. With the high angular and energy resolutions now achievable, this technique can measure the electronic structure with great precision, and thus represents the best technique choice to visualize the energy and momentum phase space of electrons.

The discovery of photoemission process can be traced back to 1839 when Alexandre Edmond Becquerel observed the photoelectric effect via an electrode in a conductive solution exposed to light [35]. In 1887, Hertz further observed the photoelectric effect along with the production and reception of electromagnetic (EM) waves [36]. But the underlined principle was not well understood until 1905 when Albert Einstein introduced the concept of light quanta – Photon [37]. A schematic of photoemission experiment is shown in Fig. 4, where we send in energetic photons to excite the electrons out of the sample, then record its emission directions and kinetic energy with an electron analyzer.

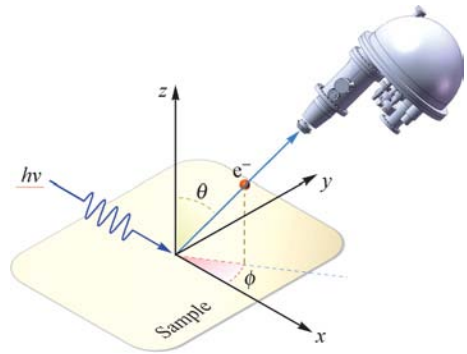


**Fig. 4** Illustration of a photoemission experiment. When we shine a light beam with the photon energy ($h\nu$) greater than the sample work function, we can observe photoemitted electrons. By using an energy analyzer with angle resolution, the energy and momentum information of the photoelectrons can be acquired.

The energetics of the photoemission process is shown in Fig. 5. In a crystal, electrons form energy bands (usually called core or valence bands depending on their energy levels), and can have non-uniform distribution of electron density of states. To study these states by photoemission process, we need impinge photons (with quantized energy $E = h\nu$) upon the sample surface to excite electrons out before they can be detected by an electron analyzer. Due to the existence of a potential barrier $\Phi$ between the Fermi-energy $E_{\rm F}$ and vacuum level $E_{\rm vac}$, the condition $h\nu > \Phi$ must be satisfied. By measuring the photoelectron kinetic energy $E_{\rm k}$, we can extract the electrons' original binding energy $E_{\rm b}$. From Fig. 5, we see the following relationship immediately as a result of energy conservation:

$$E_{\rm b} = h\nu - \Phi - E_{\rm k} \tag{1}$$

With additional information on the photoelectrons' emission angle with respect to the sample surface, we can extract the electron momentum, both parallel ($k_{//}$) and perpendicular ($k_{\perp}$) to the sample surface. Due to the existence of work function $\Phi$, an electric field exists

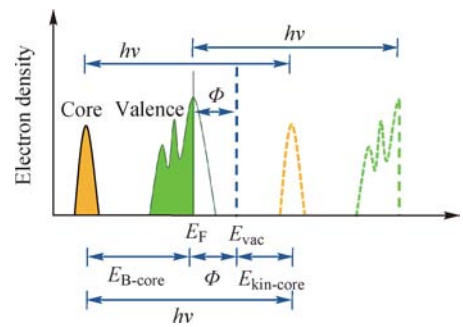


**Fig. 5** Energetics of the photoemission process. The symbols are defined as: $h\nu$ – Photon energy; $\Phi$ – Work function; $E_{\rm F}$ – Fermi energy; $E_{\rm vac}$ – Vacuum level; $E_{\rm B\text{-}core}$ – Binding energy of core level electrons; $E_{\rm kin\text{-}core}$ – Kinetic energy of photoelectrons from core level.

along the sample surface normal, thus only $k_{//}$ is conserved during the photoemission process, i.e.,

$$k_{//\text{photoelectron}} = k_{//\text{sampleelectron}} \tag{2}$$

Equations (1) and (2) show that ARPES is an ideal method for studying materials with 2D electronic structure; if it is apply to 3D materials, the work function $\Phi$ and the details of the surface field have to be understood before we reconstruct the sample's 3D electronic structure from ARPES data.

## 2.2 General principle

What we have discussed above is the energetics of the photoemission process; below we will give a brief description of the photocurrent we collect in the photoemission experiment [38].

The photoemitted electric current comes from the excitation of electrons from the initial state $|\psi_i\rangle$ to the final state $|\psi_f\rangle$ by the introduced photon field (with vector potential $\boldsymbol{A}$) associated with the interaction Hamiltonian $H_{\text{int}} = P \cdot A$, thereby the transition probability $\boldsymbol{P}$ can be computed by Fermi's Golden Rule or the first Born approximation. In the diploe approximation [76], we get

$$P \propto \frac{2\pi}{\hbar} |\langle \psi_f | H_{\text{int}} | \psi_i \rangle|^2 \delta(E_f - E_i - \hbar\omega) \tag{3}$$

To study the transition matrix element above, we have to make some assumptions about the wavefunction. The simplest approximation is to use the one-electron wavefunction for the initial and final states. For the final state, we have an additional free electron with the energy $E_k$, accordingly for a system with $N$ electrons, we can write the initial states as:

$$|\psi_i\rangle = |\phi_{i,k}\rangle |\psi^k_{i,R(N-1)}\rangle \tag{4}$$

where $|\phi_{i,k}\rangle$ is the orbital from which the photoemitted free electron is excited, and $|\psi^k_{i,R(N-1)}\rangle$ represents the remaining electrons.

In the same manner, the final state can be written as a product of the photoemitted electron and that of the remaining $N-1$ electrons:

$$|\psi_f\rangle = |\phi_{f,E_k}\rangle |\psi^k_{f,R(N-1)}\rangle \tag{5}$$

Therefore, the transition matrix element becomes

$$\begin{aligned}\langle \psi_f | H_{\text{int}} | \psi_i \rangle &= \langle \psi^k_{f,R(N-1)} \langle \phi_{f,E_k} | H_{\text{int}} | \phi_{i,k} \rangle \psi^k_{i,R(N-1)} \rangle \\ &= \langle \phi_{f,E_k} | H_{\text{int}} | \phi_{i,k} \rangle \langle \psi^k_{f,R(N-1)} | \psi^k_{i,R(N-1)} \rangle\end{aligned} \tag{6}$$

which is a product consisting of a one-electron matrix element and an $(N-1)$ electron overlap integral. If, for simplicity, we assume that the remaining $(N-1)$ orbitals are the same for the initial and final state (the frozen-orbital or sudden approximation), i.e., $|\psi^k_{i,R(N-1)}\rangle = |\psi^k_{f,R(N-1)}\rangle$, Then $\langle \psi^k_{f,R(N-1)} | \psi^k_{i,R(N-1)} \rangle = 1$ and the transition matrix element $\langle \psi_f | H_{\text{int}} | \psi_i \rangle = \langle \phi_{f,E_k} | H_{\text{int}} | \phi_{i,k} \rangle$, which is just the one-electron matrix element. Under this assumption, the PES experiment measures the negative Hartree–Fock orbital energy, and the experimental spectra will be given by the delta functions [Fig. 6(b)] that trace the real band dispersion [Fig. 6(a)].

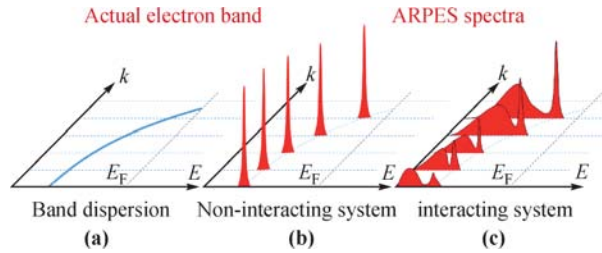


**Fig. 6** Spectra of ARPES. **(a)** True dispersion of an electron band. **(b)** Momentum resolved ARPES spectra from a non-interacting electron system. **(c)** Momentum resolved ARPES spectra from an interacting electron system.

As the TIs currently under investigations are mostly weakly interacting systems, the single particle picture discussed above can be applied well. The ARPES results then on the whole represent the real band structure of these TI materials.

In other materials where the electron–electron interaction is strong, however, the situation is more complicated. After the photoemission, the remaining $(N-1)$ electron system is not necessarily left in its ground state, thus the system will readjust its charge distribution and minimize its energy. Let us assume the final $(N-1)$ electrons has $S$ excited states, $|\psi^k_{f,S(N-1)}\rangle$, with energy $E_{S(N-1)}$, the probability that the system is remained in the excited $S$ is $|\langle \psi^k_{f,S(N-1)} | \psi^k_{i,R(N-1)} \rangle|^2$, thus the total photocurrent measured by the experiment is the sum over the contributions of all the possible final states:

$$\begin{aligned} I \propto & \sum_{f,i,k} |\langle \phi_{f,E_k} | H_{\text{int}} | \phi_{i,k} \rangle|^2 \\ & \cdot \sum_S |\langle \psi^k_{f,S(N-1)} | \psi^k_{i,R(N-1)} \rangle|^2 \\ & \cdot \delta(E_{f,E_k} + E_{S(N-1)} - E_{0(N)} - \hbar\omega) \\ \triangleq & \sum_{f,i,k} |\langle \phi_{f,E_k} | H_{\text{int}} | \phi_{i,k} \rangle|^2 A(k,E) \end{aligned} \tag{7}$$

where

$$\begin{aligned} A(k,E) = & \sum_S |\langle \psi^k_{f,S(N-1)} | \psi^k_{i,R(N-1)} \rangle|^2 \\ & \cdot \delta(E_{f,E_k} + E_{S(N-1)} - E_{0(N)} - \hbar\omega) \end{aligned} \tag{8}$$

is the spectral function for the wave number $k$ and energy $E$ which describes the probability of removing $(E < E_F)$ or adding $(E > E_F)$ an electron with the energy $E$ and wave vector $k$ from or to the interacting $N$-electron system. In this case, the PES spectra will become more complicated and the $\delta$ function like PES peaks will be accompanied with the satellite peaks [Fig. 6(c)].

By definition, the spectra function $A(k, E)$ can be related to the single-particle Green's function by

$$A(k, E) = \frac{1}{\pi}|\mathrm{Im}(G(k, E))| \tag{9}$$

For a non interacting system with the one-electron energy $E_k^0$, the Green's function is the following:

$$G_0(k, E) = \lim_{\epsilon \to 0} \frac{1}{E - E_k^0 - \mathrm{i}\epsilon} \tag{10}$$

thus

$$A_0(k, E) = \delta(E - E_k^0) \tag{11}$$

which again tells us that the spectral function is a $\delta$ fucntion at $E = E_k^0$, agreeing with our previous discussion on the non-interacting systems.

In an interacting system, however, the electron energy gets renormalized by the self energy $\Sigma(k, E)$, which makes the Green's function becomes

$$G(k, E) = \frac{1}{E - E_k^0 - \Sigma(k, E)} \tag{12}$$

and

$$A(k, E) = \frac{1}{\pi}\left|\frac{\mathrm{Im}[\Sigma(k, E)]}{\{E - E_k^0 - \mathrm{Re}[\Sigma(k, E)]\}^2 + \{\mathrm{Im}[\Sigma(k, E)]\}^2}\right| \tag{13}$$

Therefore, for the study of future TI materials with strong correlation, such as the Ir-related compounds recently proposed [39, 40], the more sophisticated treatment on the ARPES spectra as above should be applied before the real band structure can be deduced from the experimental measurements.

### 2.3 Experimental setup for angle resolved photoemission spectroscopy

The light sources for ARPES vary a lot in forms and in the experimental side, a basic photoemission ARPES station usually comprises the following four elements: i) Vacuum system, ii) Photon source, iii) Electron analyzer, iv) Sample manipulating/cooling system. Figure 7 shows a typical ARPES spectrometer. There can also be other accessaries attached to the chamber for sample surface preparation, but the four parts mentioned above are the necessary ones for all ARPES spectrometer. In the following, we will briefly introduce the function of each part.

(i) Vacuum system

The vacuum system is the housing of the whole spectrometer, which usually consists of a vacuum chamber and the supporting pump system. Reducing the residue gas molecules in the chamber is necessary as they not only contaminate the sample surface, but also scatter the photoelectrons and prevent them from reaching the detector.

Depending on the materials studied, the vacuum requirement for photoemission measurements can be very different, ranging from $10^{-7}$ Torr for regular gas phase to $10^{-11}$ Torr for solid state samples so as to allow enough data collection time before the sample surface is contaminated by adsorpted residue gas molecules.

(ii) Light sources

A light source is required for any ARPES spectrometer. It produces photons for exciting the photoemission process. For gas phase photoemission experiments, the energy of the photons must exceed the lowest binding energy; while for the solid state ARPES measurements, it must be larger than the working function of the materials. The light sources for ARPES vary much in forms and operating principles. Commonly used sources include X-ray tube [41], gas discharge lamp [42], synchrotron radiation [43] and laser [44].

Due to its brightness and the capability of adjusting photon energy in a broad range (from a few eVs to

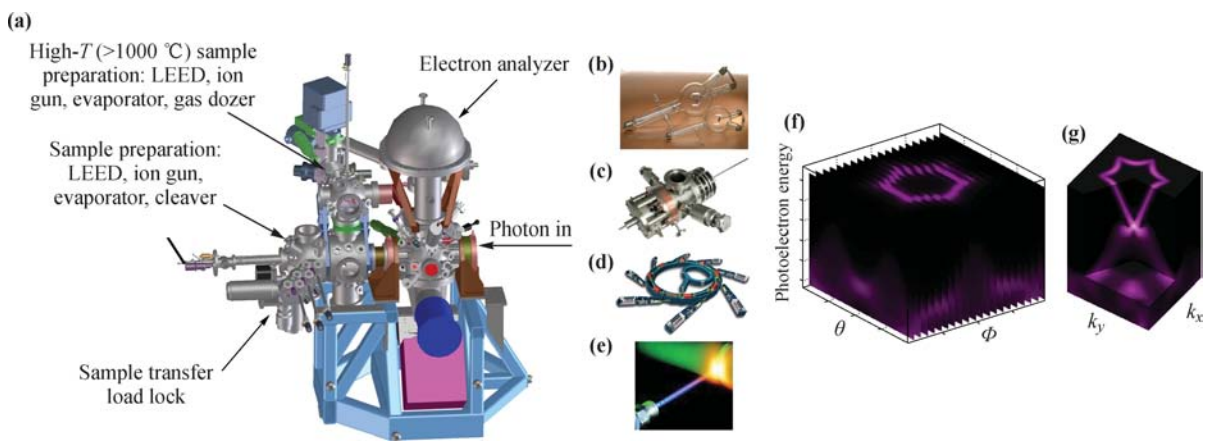


**Fig. 7** Illustration of an ARPES endstation and sample data. **(a)** Schematic (courtesy J. Pepper) of the High energy resolution spectrometer (HERS) endstation at the advanced light source (ALS) of Lawrence Berkeley National Lab (LBNL), with the rotating analyzer scheme (see text). **(b)**–**(e)** Different types of photon sources: (b) X-ray tube; (c) Gas discharge lamp; (d) Synchrotron and (e) Laser. **(f)** An example of combining 2D dispersions cuts to reconstruct the 3D band structure. **(g)** Reconstructed 3D dispersion in $k$-space with fine sampling along $\Phi$ direction (data from Ref. [16]).

hundreds of eVs), synchrotron-radiation became the most popular light source. A synchrotron has a storage ring for electrons and several bending magnets or undulators. Since the charged particle emit electromagnetic radiation when accelerated [45], people purposely bend the trajectory (by magnet or undulator) of electrons in the storage ring to get the electromagnetic radiation (A more detailed description of synchrotron can be found in Ref. [46].).

(iii) Electron analyzer

After the electrons in the sample are photoemitted, an electron analyzer collects them and measures their energy and emission direction for extracting the electron momentum. At present, 2D electrostatic spherical deflection analyzer (SDA) is the most commonly used analyzer in most ARPES stations, which can acquire two-dimensional information in a single measurement.

The schematics of a typical SDA analyzer is shown in Fig. 8, which consists of two concentric hemispheres. For transmission of electrons with initial energy $E_0$ along the central path with $R_0 = (R_{\rm in} + R_{\rm out})/2$, the potential of the outer hemisphere has to be $V_{\rm out} = E_0[3-2/(R_0/R_{\rm out})]/e$, and that of the inner hemisphere $V_{\rm in} = E_0[3-2/(R_0/R_{\rm in})]/e$. For electrons with energy slightly higher/lower than $E_0$, the trajectory will be closer to the outer/innner hemisphere, respectively. Thus the electrons of different energy will disperse along the longitudinal direction of the detector [Fig. 8(a)]. Almost all SDA analyzers use an additional pre-retardation stage prior to the energy analysis, enabling the analyzer to measure a larger energy range and improve the resolution for high energy electrons (Likewise, after the pre-retardation, a lower pass energy mode can be used.).

In addition to the energy detection, modern SDA analyzer can also collect electrons' angle information by focusing electrons from different emission angle to different spacial points. As can be seen in Fig. 8(a), where the front retardation lens can preserve the angular information of the incoming electrons, which will arrive at different lateral positions of the detector. As the angle and energy dispersion of electrons on the detector are perpendicular, a single measurement of the SDA analyzer can acquire a 2D dispersion of the band structure.

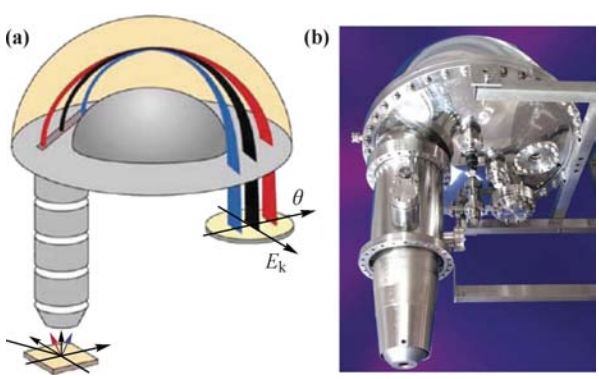


**Fig. 8** Schematics **(a)** and real image **(b)** of a SDA type analyzer, SES R4000 from Gamadata Scienta. Photoelectrons emitted from the sample are first retarded by the pre-retardation lens before entering the centripetal field region (produced by the two cocentric hemispheres) for the energy analysis (energy dispersion is along the $E_{\rm k}$ axis, see left panel). Electrons with different emitting angle can be focused to different spacial locations (along $\theta$ axis) perpendicular to the energy dispersion direction.

Figure 8(b) shows a real SDA analyzer (Scienta R4000) in which the hemispherical lens cover and the pre-lens in front can be clearly seen. This is the analyzer we use the most for the ARPES study that we will present in the latter part of this review.

(iv) Sample manipulating/colling system

Consider that a typical SDA electron analyzer only gets a 2D dispersion cut during each measurement, to acquire the 3D electronic structure, we have to sample the data along the 2nd direction perpendicular to the lateral direction of the 2D SDA detector (the $\Phi$ angle, see right panel of Fig. 7). It is obvious that if the sampling step of the $\Phi$ angle becomes smaller, we can get finer momentum information along this direction – at the cost of longer data acquisition time. The right panel of Fig. 7 shows a typical set of ARPES data from HERS that directly visualize the electron structures in the sample.

To realize the sampling in $\Phi$ direction, one has two choices: rotating the sample or rotating the analyzer. Rotating the sample seems a much easier way (as it is much smaller than the analyzer) and it is in fact more commonly adopted. However, it has some disadvantages: First, as the relative orientation of the sample and light beam is changed during this rotation, the matrix elements [Eq. (6)] also change, making it harder to interpret the data. Second, for samples with multiple domains or rough surface, the light beam can be blocked by extruded parts on the surface when the sample rotates. Third, due to the inevitable error of the concentricity of the manipulator, for small samples and multi-domain samples, rotation of the sample often causes the photon beam to miss the sample or to shine at different domains.

To overcome these disadvantages, sometimes we need to adopt the rotating analyzer scheme, even though it is technically harder due to the large size of the analyzer and the difficulty to maintain the ultra-high vacuum during the rotation. Nevertheless, we managed to address these technical issues and realize it in HERS endstation.

Finally, as the high resolution ARPES measurements have to be performed at low temperature to reduce the thermal broadening effect ($\sim k_{\rm B}T$) [47], a sample cooling system (that can reach the temperature region where $k_{\rm B}T$ is comparable to the analyzer energy resolution) is also needed. Obviously, in addition to reducing the temperature broadening, the cooling system will also be helpful in the study of low temperature electronic structures.

## 3 Electronic structure of 3D topological insulators (TIs)

After the prediction of 3D TI materials, ARPES was soon applied to these candidates and yielded fruitful results [5–28]. Many of the materials have been confirmed to be 3D TIs with their unique electronic structure with an odd number of Dirac fermions on the surface with helical spin structure protected by the time reversal symmetry. Furthermore, the rich information acquired by ARPES has helped the understanding of other experimental techniques such as electric transport, STM. In the following, a few examples are presented to demonstrate the rich unusual properties of 3D TIs.

### 3.1 $Bi_xSb_{1-x}$ alloy

$Bi_{1-x}Sb_x$ alloy was first proposed to be a 3D TI within the doping range $0.07 < x < 0.22$ in the pioneering work on the band theory of 3D TIs [6], as is illustrated in Fig. 9 that summarizes the evolution of the $Bi_{1-x}Sb_x$ band structure.

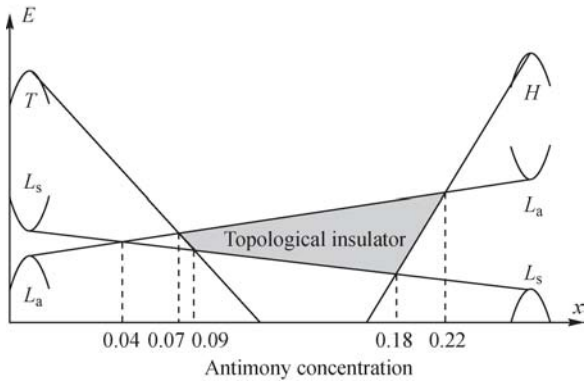


**Fig. 9** Schematic of the band evolution of $Bi_{1-x}Sb_x$ alloy as a function of antimony conentration ($x$). Reproduced from Ref. [6], Copyright © 2007 American Physical Society.

Pure Bismuth is a semimetal with strong spin-orbital coupling, and the overlap between the bands around $L$ points and that at $T$ point leads to the simultaneous existence of electron and hole pockets at $E_F$ (left most axis of Fig. 9). The substitution of Bismuth by Antimony results in the downshift of the $T$ and $L_s$ bands and the upshift of the $L_a$ band, thus the direct bulk gap at the $L$ points diminishes with the Antimony concentration and eventually vanishes at ($x \approx 0.04$). Further Antimony doping makes the gap turn negative, but the bulk semimetalicity remains since the $T$ band is still above the $L$ bands. When $x \gtrsim 0.07$, the $T$ band falls below the $L_s$ band, turning the system to a semiconductor with an inverted band gap between $L_a$ and $L_s$ bands. The semiconductor state persists till $x \approx 0.22$, when another band around $H$ point crosses the $L_s$ band, converting the system back to a semimetal.

Due to the inverted band structure and the opening of the bulk gap, $Bi_{1-x}Sb_x$ was predicted [6] to be a (strong) 3D TI in the semiconductor region ($0.07 < x < 0.22$) with an odd number of the $E_F$ crossings of its surface state between the two time invariant point $\Gamma$ and $M$.

The ARPES experiments were soon carried out [12] (Fig. 10), and the surface state bands of $Bi_{0.9}Sb_{0.1}$ was shown to cross $E_F$ five times [The $E_F$ crossing points 4 and 5 are seen in the plot of the second derivative of the ARPES intensity spectra, Fig. 10(b).]; the subsequent spin resolved measurements [48, 76] also indicated the non-degenerate spin polarization of the surface state (at least at the $E_F$ corssings 1–3), and the bulk gap of the studied sample was estimated to be $\sim 50$ meV at the $M$ point of the surface Brillouin zone (BZ).

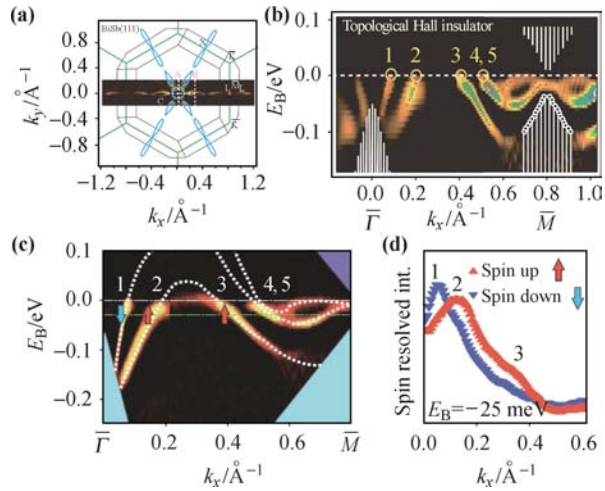


**Fig. 10** **(a)** ARPES intensity map at $E_F$ for $Bi_{0.9}Sb_{0.1}$. **(b)** The surface-band-dispersion (second-derivative) image along $\Gamma$–$M$ direction, showing five $E_F$ crossings from $\Gamma$ to $M$ points. The shaded white area shows the projection of the bulk bands based on ARPES data, as well as a rigid shift of the tight binding bands to sketch the unoccupied bands above the Fermi level. Reproduced from Ref. [12], Copyright © 2008 Nature Publishing Group. **(c, d)** Surface band dispersion image along $\Gamma$–$M$ direction (c) with the spin polarization (d), reproduced from Ref. [48], Copyright © 2009 American Association for the Advancement of Science.

Although the $Bi_{1-x}Sb_x$ alloy shows an odd number of Fermi-crossings, its complicated band structure [five Fermi-crossings in total, with that of 4, 5 very close to each other thus making the spin signature vanish in the measurement shown in Fig. 10(d)] and the small energy gap ($\sim 50$ meV) made it highly desirable to search for simpler 3D TI materials with the signature of Dirac fermions explicit (ideally with a single Dirac fermion on the surface – similar to the simplicity of Hydrogen atom in atomic physics) and a larger bulk gap. Materials with these nice characters will facilitate not only the realization of many non-trival topological phenomena, but also their potential applications.

Under this circumstance, a family of single dirac cone TIs with a large bulk gap in $V_2$–$VI_3$ materials were soon put on the table.

### 3.2 Single Dirac cone TIs from $V_2$–$VI_3$ compounds

After theoretical analysis and *ab initio* calculations, three layered materials $Bi_2Te_3$, $Bi_2Se_3$ and $Sb_2Te_3$ from the $V_2$–$VI_3$ family were proposed to be 3D TIs [13]. Better than the $Bi_{1-x}Sb_x$ alloy discussed above, these new family of 3D TIs are stoichiometric semiconductors with a single in-gap surface Dirac fermion located at the $\Gamma$ point of the surface BZ. The bulk energy gap of this family of materials is also much larger (up to ~300 meV in $Bi_2Se_3$) than the energy scale of room temperature (~ 30 meV) and that found in the $Bi_{1-x}Sb_x$ alloy (~ 50 meV).

The underlined physics of these materials can be explained by a simple effective model of four bands [13]. In short, the strong spin–orbit interaction in these materials causes the inversion of the Bismuth/Antimony and Selenium/Tellurium $P_z$ orbitals, resulting in the bulk gap and a single in-gap Dirac fermion centered at the $\Gamma$ point. The simplicity of a single surface Dirac cone makes this family of materials ideal candidates for realizing the many proposed topological phenomena, such as the magneto–electric effect [7]; and the large bulk gap (compared to the energy scale of room temperature) makes them possible candidates for high temperature spintronics applications.

The non-trivial band structures of these materials were soon confirmed by ARPES studies. The characteristic Dirac fermions at the BZ center and the large bulk gap were observed in all the three compounds [14, 16, 49]. With such properties and application potentials, this family of materials are now under intensive investigations. In the following, we will use two examples ($Bi_2Te_3$ and $Bi_2Se_3$) to demonstrate their unique band structures and the non-trivial surface state properties.

The band structure of $Bi_2Te_3$ is shown in Fig. 11. Besides the bulk conduction and valance bands, the single Dirac cone is clearly seen [panel (a) and (c)] at the center of the BZ, whose surface nature is confirmed by the energy dependent ARPES study [panel (d)]. The indirect bulk gap measured is ~ 165 meV, and the velocity of the Dirac fermion is $\sim 4 \times 10^5$m/s, about half of that of graphene [16].

Due to the vacancies and defects in the crystal, as grown $Bi_2Te_3$ samples usually have excess n-type carriers in bulk [16], as is indicated by the small BCB pocket in the ARPES measurement (Fig. 11).

To realize the topological insulating phase (tune $E_F$ into the gap), one can either reduce these imperfections by tuning the crystal growth condition, or by doping holes into the material to compensate for these excess n-type carriers. So far both methods have been successfully implemented and Fig. 12 and Fig. 13 [16] show two such examples, respectively. For the bulk doping method, introduction of more hole concentrations can further drive the material into p-type [Fig. 13(d)], making many applications feasible such as topological p–n junction. We note that unlike the surface state of regular materials that is extremely sensitive to impurities, the topological surface state in $Bi_2Te_3$ persists in all doping regions (Fig. 13) as long as the dopants are

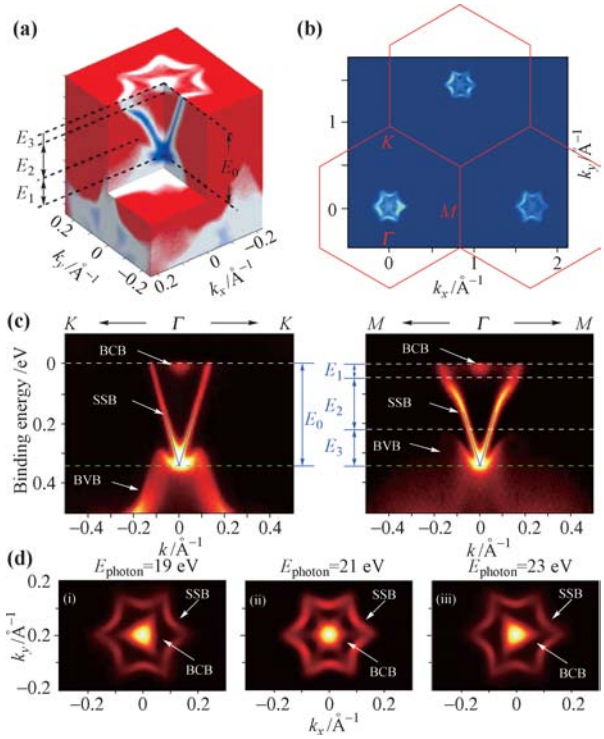


**Fig. 11** **(a)** The 3D band structure of as grown $Bi_2Te_3$. **(b)** Broad FS map covering three BZs, where the red hexagons represent the surface BZ. The uneven intensity of the FSs at different BZs results from the matrix element effect. **(c)** ARPES measurements of band dispersions along $K$–$\Gamma$–$K$ (left) and $M$–$\Gamma$–$M$ (right) directions (Reproduced from Ref. [16], Copyright © 2009 American Association for the Advancement of Science.). The broad bulk conduction band (BCB), bulk valance band (BVB) and the sharp V-shape linear dispersion from the Dirac surface state band (SSB) are labeled. The apex of the V-shape SSB dispersion is the Dirac point. The bulk energy gap is ~ 0.165 eV. **(d)** Photon energy dependent FS maps. The shape of the inner FS changes markedly with photon energies, indicating a strong $k_z$ dependence due to its bulk nature as predicted in bulk calculation [16], whereas the non-varying shape of the outer hexagram FS confirms its surface state origin.

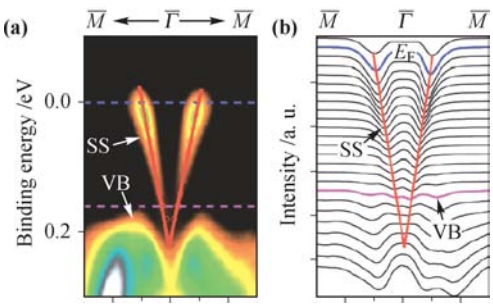


**Fig. 12** Band structure of $Bi_2Te_3$ along $M$–$\Gamma$–$M$ direction, showing an in-gap $E_F$, **(a)** ARPES intensity plot, **(b)** Momentum distribution curves. Reproduced from Ref. [77], Copyright © 2010 Wiley-VCH Verlag GmbH & Co. KGaA.

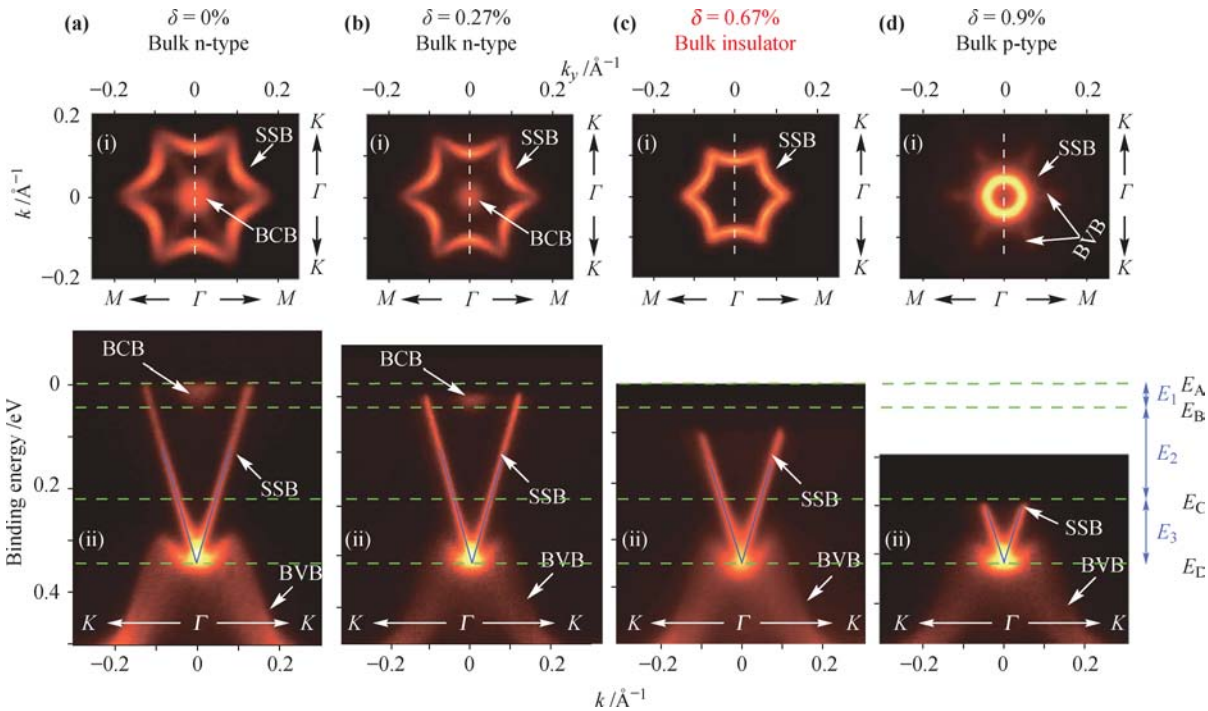


**Fig. 13** Doping dependence of FSs and $E_F$ positions. **(a)–(d)** Measured FSs and band dispersions for 0, 0.27, 0.67, and 0.9 percent nominally doped samples. Top row: FS topology (symmetrized according to the crystal symmetry). The FS pocket formed by SSB is observed for all dopings; its volume shrinks with increasing doping, and the shape varies from a hexagram to a hexagon from (a) to (d). The pocket from BCB also shrinks upon doping and completely vanishes in (c) and (d). In (d), six leaf-like hole pockets formed by BVB emerge outside the SSB pocket. Bottom row: image plots of band dispersions along $K$–$\Gamma$–$K$ direction as indicated by white dashed lines superimposed on the FSs in the top row. The EF positions of the four doping samples are at 0.34, 0.325, 0.25, and 0.12 eV above the Dirac point, respectively. Reproduced from Ref. [16], Copyright © 2009 American Association for the Advancement of Science.

non-magnetic, due to the protection of time reversal symmetry (as will be discussed later).

The spin polarization of $Bi_2Te_3$ surface state was also investigated with the spin-resolved ARPES (Fig. 14) [15], which has confirmed its unique helical structure.

Despite the overall agreement with theoretical predictions, the experiments revealed a surprise. From Fig. 11 and Fig. 13, we see that the FS of the surface Dirac fermion shows an hexagram shape in conflict with the circular shape predicted by simple $k\cdot$ Hamiltonian. This unconventional warping of the surface state FS [Fig. 11(b)] provides an intrinsic test for the topological theory. To look into this discrepancy, an additional third order term was added into the surface Hamiltonian (Ref. [19] and others) to explain the hexagonal warping effect.

The validity of the revised model can be further checked by the observable consequences it predicts, such as the surface quasi-particle interference and the out of plane surface spin polarization. Both effects were soon observed by scanning tunneling microscopy (STS) [50] and the spin-ARPES measurement [51, 52].

The band structure of another compound in the family, $Bi_2Se_3$, is shown in Fig. 15 [14, 16]. Similar to $Bi_2Te_3$, there is a surface Dirac cone centered at the $\Gamma$ point. The bulk gap ($\sim$ 200 meV) of $Bi_2Se_3$ is slightly larger than that of $Bi_2Te_3$; and unlike $Bi_2Te_3$ where the Dirac point is below the valence band top, the Dirac point of $Bi_2Se_3$ is "exposed" and resides at the top of the bulk valence

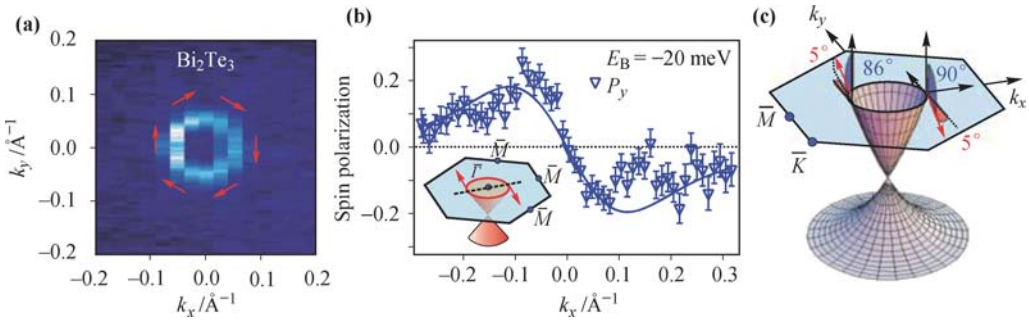


**Fig. 14** **(a)** FS map of $Bi_2Te_3$, **(b)** Measured $y$-component of spin-polarization along the $\Gamma$–$M$ direction; inset shows the schematic of the cut direction. **(c)** Fitted spin polarization vector $P(S_x, S_y, S_z)$ are $(\sin 90^\circ \cos(-95^\circ), \sin 90^\circ \sin(-95^\circ), \cos 90^\circ)$ for electrons with $+k_x$ and $(\sin 86^\circ \cos 85^\circ, \sin 86^\circ \sin 85^\circ, \cos 86^\circ)$ for electrons with $-k_x$, demonstrating the topological helicity of the Dirac cone. Reproduced from Ref. [15], Copyright © 2009 Nature Publishing Group.

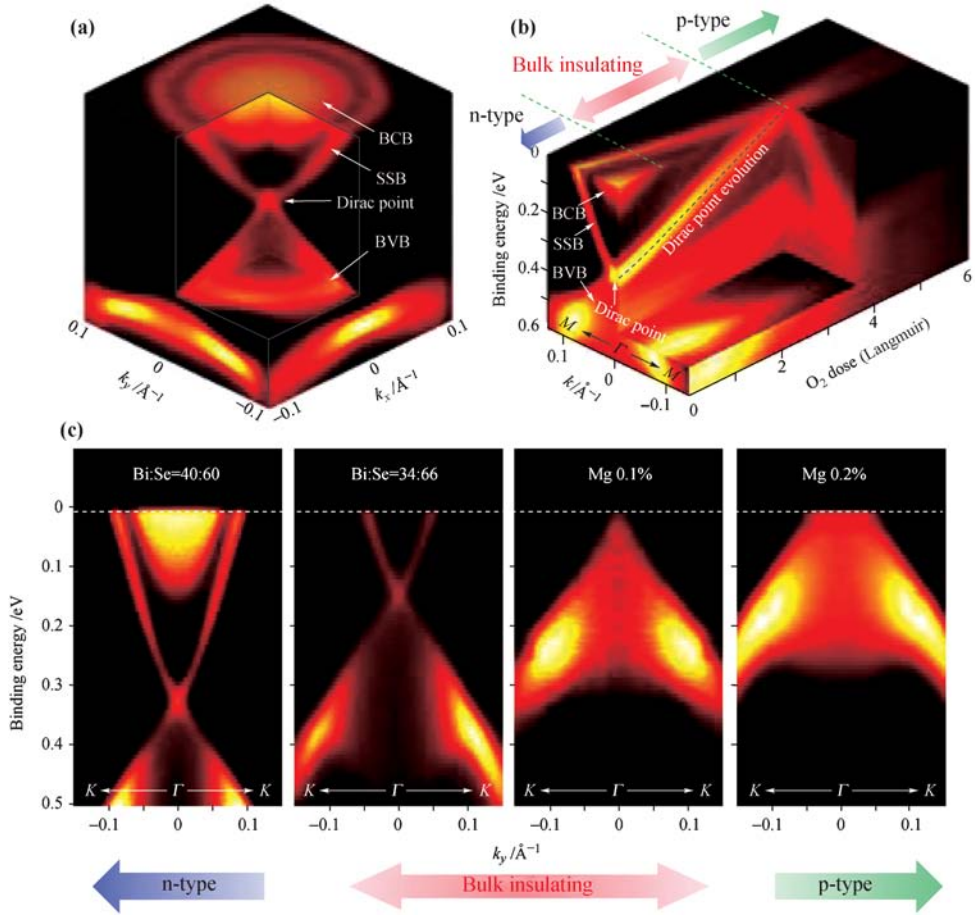


**Fig. 15** **(a)** 3D band structure of $Bi_2Se_3$, **(b)** Evolution of the band structure (along $M$–$\Gamma$–$M$ direction) by photon assisted surface doping with $O_2$ (Langmuir, a unit measuring the exposure to a surface, is defined as the product of the gas pressure and the exposure time; 1 L = 1e-6 Torr. Second.). Blue dashed line traces the upshift of the Dirac point with the $O_2$ doping. Green dashed lines indicate the dosages that separate the three doping regions: At 0.95 L, the BCB bottom reaches $E_F$; at 3.6 L, the Dirac point reaches $E_F$; and beyond 3.6 L, the Dirac point is above $E_F$. **(c)** With bulk doping, the band structure evolution from n-type (first panel, sample melt composition $Bi_2Se_3$) to p-type (fourth panel, $(Bi_{0.998}Mg_{0.002})_2Se_3$) through the bulk insulating region (2nd panel, $Bi_{1.7}Se_{3.3}$) and the topological transport (3rd panel, $(Bi_{0.999}Mg_{0.001})_2Se_3$) point. Reproduced from Ref. [25], Copyright © 2010 American Association for the Advancement of Science.

band [16]. This exposure of the Dirac point makes it the easiest to observe the unique phenomena happening at the topological transport point when $E_F$ coincides with the $E_{\text{Dirac point}}$, at which $k_f = 0$ and there is no interference from the bulk carriers. Similar to $Bi_2Te_3$, by surface [Fig. 15(b)] or bulk doping [Fig. 15(c)], $E_F$ can be tuned to make the bulk crystal either p- or n-types, or at the topological transport point.

Due to the finite extension of the surface state [54], when the thickness of the $Bi_2Se_3$ crystal becomes comparable to the surface state wave function, the surface state from the top and bottom surfaces can overlap, leading to an opening of a gap at the Dirac point due to their interaction. The effect is shown in the ARPES, resulting from MBE grown $Bi_2Se_3$ thin films (Fig. 16) where the thickness of the samples can be precisely controlled.

### 3.3 Effects of non-magnetic and magnetic impurities

Comparing to the surface state of regular materials (e.g. crystals of noble metal and some insulators such as Si), which is usually very fragile and sensitive to external perturbations such as impurities, the Dirac surface state of TIs are unusually robust. This robustness originates from the topology of its bulk electronic structure and is thus protected by TRS. As a consequence, in the presence of TRS, the massless surface Dirac fermions of TIs will persist against any impurities or crystal defects as long as the topology of the bulk band structure of the crystal does not change.

To test this ususual property, one can purposely introduce non-magnetic impurities into the bulk or onto the surface to verify the robustness of the massless surface Dirac cone. The existence of a continuous Dirac point that connects the upper and lower surface Dirac cones [Fig. 17(b)] should not be broken even if the system is severely perturbed by non-magnetic dopants [Fig. 17(a)]. As we will see below, the ARPES experiments carried out on both the bulk and surface doped $Bi_2Se_3$ have confirmed this TRS protection.

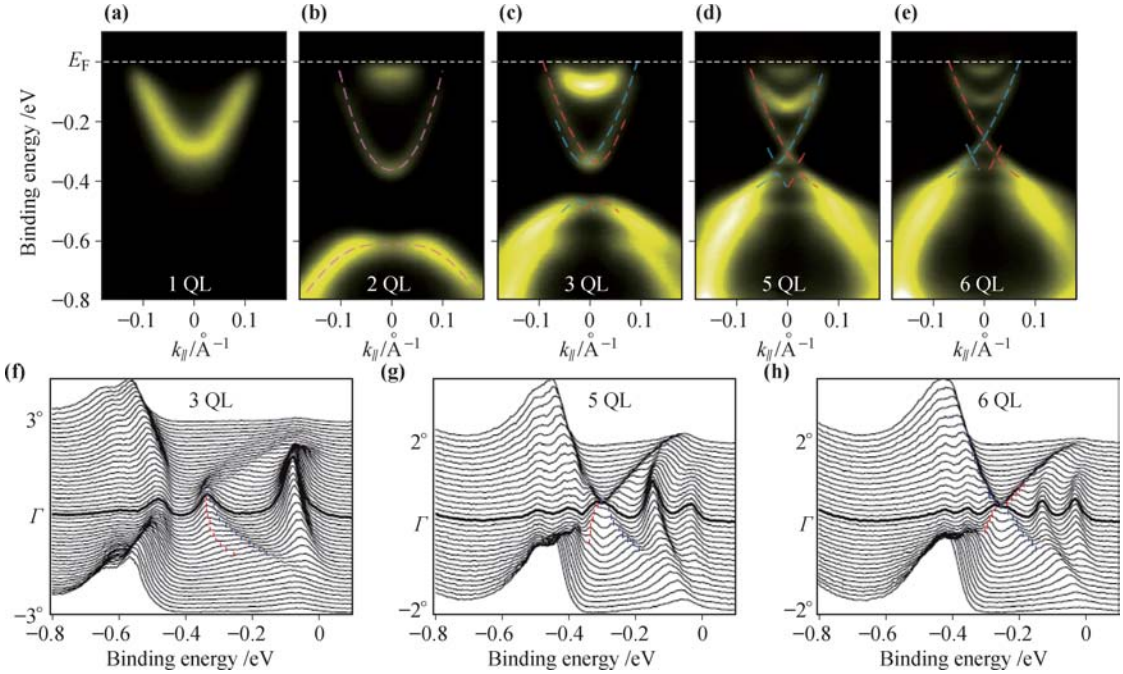


**Fig. 16** ARPES spectra of $Bi_2Se_3$ films at room temperature. **(a)**–**(e)** ARPES spectra of 1, 2, 3, 5 and 6 quintuple layers (QLs) along the $\Gamma$–$K$ direction measured at room temperature. **(f)** EDCs of (c). **(g)** EDCs of (d). **(h)** EDCs of (e). The pink, blue and red dashed lines in (b)–(e) represent the fitted curves. Reproduced from Ref. [53], Copyright © 2010 Nature Publishing Group.

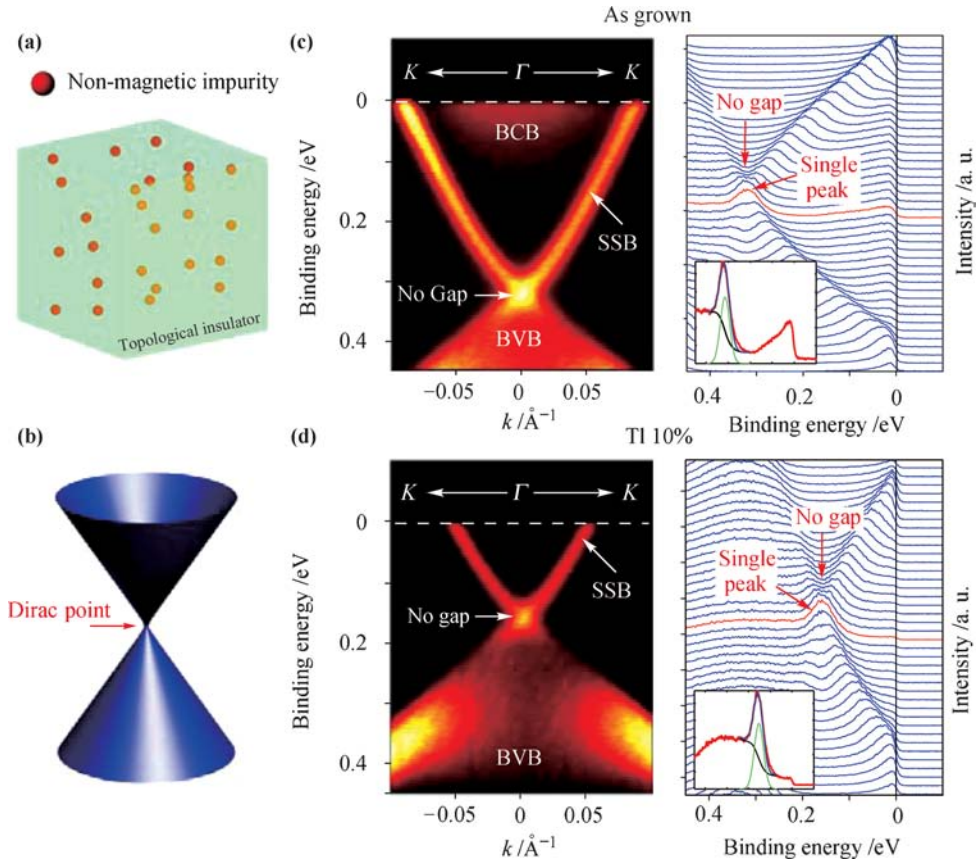


**Fig. 17** **(a, b)** A nonmagnetically doped TI with a Dirac point connecting the upper and lower Dirac cones as in the undoped case. **(c)** Band structure along the $K$–$\Gamma$–$K$ direction of undoped $Bi_2Se_3$. Left and right subpanels show the ARPES spectral intensity plot and a stacking plot of the energy distribution curves (EDCs), respectively. The red curve in the right subpanel indicates the EDC at the $\Gamma$ point. Inset: EDC at the $\Gamma$ point (*red*), fitted with a Lorentzian peak (*green*) on the Shirley background (*black*); the total fitting function is shown in blue. The same convention is used in (d). **(d)** Band structure for a TI-doped sample, $(Bi_{0.9}Tl_{0.1})_2Se_3$. The Dirac point remains continuous. Reproduced from Ref. [25], Copyright © 2010 American Association for the Advancement of Science.

A bulk example is shown in Figs. 17(c) and (d) on non-magnetically doped $Bi_2Se_3$, where the band structures of an intrinsic and a Thulium doped samples are shown, respectively (for more examples, see Ref. [25]). In both cases, the continuity at the Dirac point is indicated by the strong spectral intensity (left sub-panels) and the single peak structure of the energy distribution curve (EDC) at the Dirac point (right sub-panels). In Fig. 17(d), the charge doping effect of Thulium is clearly seen from the dramatic shift of $E_F$ into the bulk gap. Nonetheless, the topology of the surface Dirac cone remains the same with a continuous Dirac point.

Besides the bulk, the perturbation can also be applied directly onto the TI surface. As an example, in Fig. 18, we demonstrate a dramatic treatment of the the $Bi_2Se_3$ surface by photo-assisted oxygen deposition. The accumulation of the Oxygen on the sample surface is clearly reflected by the valence spectra evolution in Fig. 18(a). The surface state and bulk valence band spectra from five different Oxygen dosage are shown in Fig. 18(b). We can see that with the increase of the Oxygen doping, the valence band dispersion of $Bi_2Se_3$ gradually deteriorates (bottom row), while the surface Dirac state persists (top row) despite the strong hole-doping effect of Oxygen, indicating its robustness (Note that the broadening of the surface state dispersion is due to the scattering of photoelectron from the increasing surface impurities such as adsorbed Oxygen and oxides.).

However, if we introduce magnetic impurities into the system, the TRS can be broken, thus the protection of the Dirac point is lifted [Fig. 19(a)], resulting in a gap that separates the upper and lower branches of the Dirac cone that makes the Dirac fermion massive [Fig. 19(b)]. This effect is illustrated in the band structure of an Fe-doped sample [Fig. 19(c)]. Unlike the non-magnetically doped cases [Fig. 17(c), (d)], the SSB dispersion at the Dirac point is broken, as indicated by the suppressed intensity regions in the spectral density plots (left sub-panels) and the twin-peak structure around the Dirac point in the EDC plots (right sub-panels).

Given the SSB gap formation at the Dirac point with broken TRS, we can further realize the insulating massive Dirac fermion state, a state capable of hosting many novel topological phenomena [7, 55–57]. To do so, we need to tune the $E_F$ into this gap, which can be achieved by Manganese doping, as Manganese dopants not only introduce magnetic moments into the system, but also naturally p-dope the samples to lower the $E_F$ (as Manganese has one less valance electron than Bi). The measurements on an optimally Mn-doped sample clearly show that the $E_F$ resides right inside the SSB gap [Fig. 19(d), left panel] of at least 7 meV [Fig. 19(d) right panel], indicating the full realization of the insulating massive Dirac fermion state in this material.

To maintain this insulating massive Dirac fermion state at higher temperatures, a further increase of the Dirac gap is required (while keeping $E_F$ inside it). However, because of the hole–doping effect of Manganese dopants, one cannot simply increase the Manganese concentration in $(Bi_{1-\delta}Mn_\delta)_2Se_3$ to acquire a larger Dirac gap, as the system will become p-type before the gap magnitude increases appreciably [25]. Instead, one can

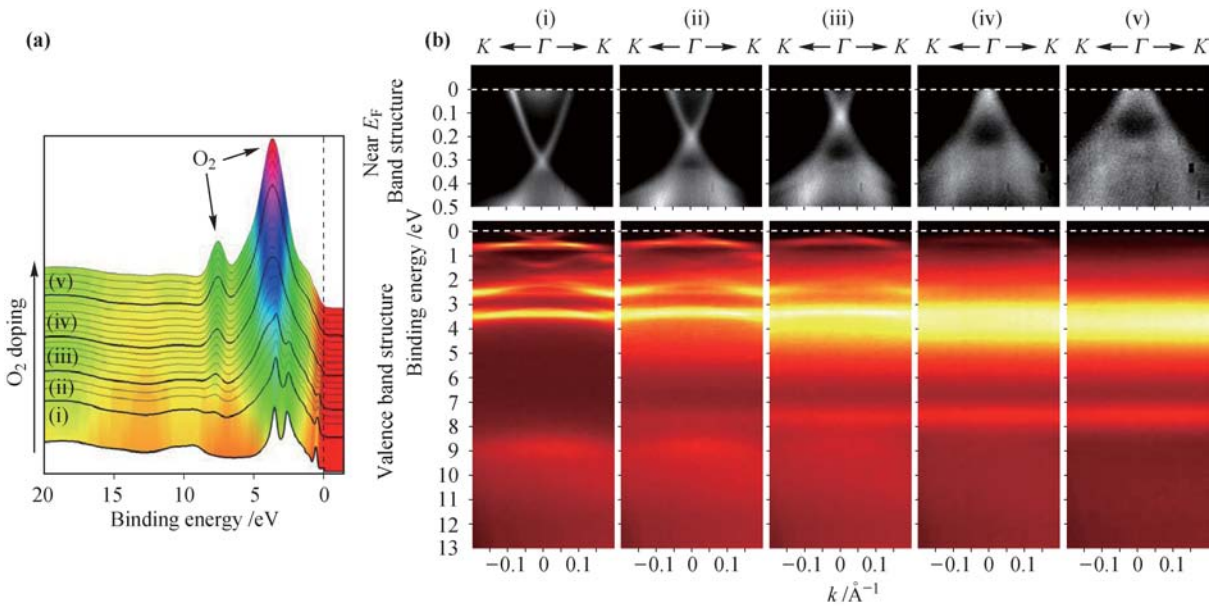


**Fig. 18** Evolution of the band structure of $Bi_2Se_3$ during photon-assisted $O_2$ surface doping. **(a)** EDC stacking plot of the integrated valance band photoemission spectra at different $O_2$ dosages. Five bold curves marked as (i)–(v) correspond to the dosages of the spectra shown in (b). The growth of the additional EDC peaks resulted from $O_2$ doping are evident from (i) to (v). **(b)** ARPES spectral intensity plots (i–v) for the near $E_F$ (top row) and valance band (bottom row) maps at the five $O_2$ dosages indicated in (a). Reproduced from Ref. [25], Copyright © 2010 American Association for the Advancement of Science.

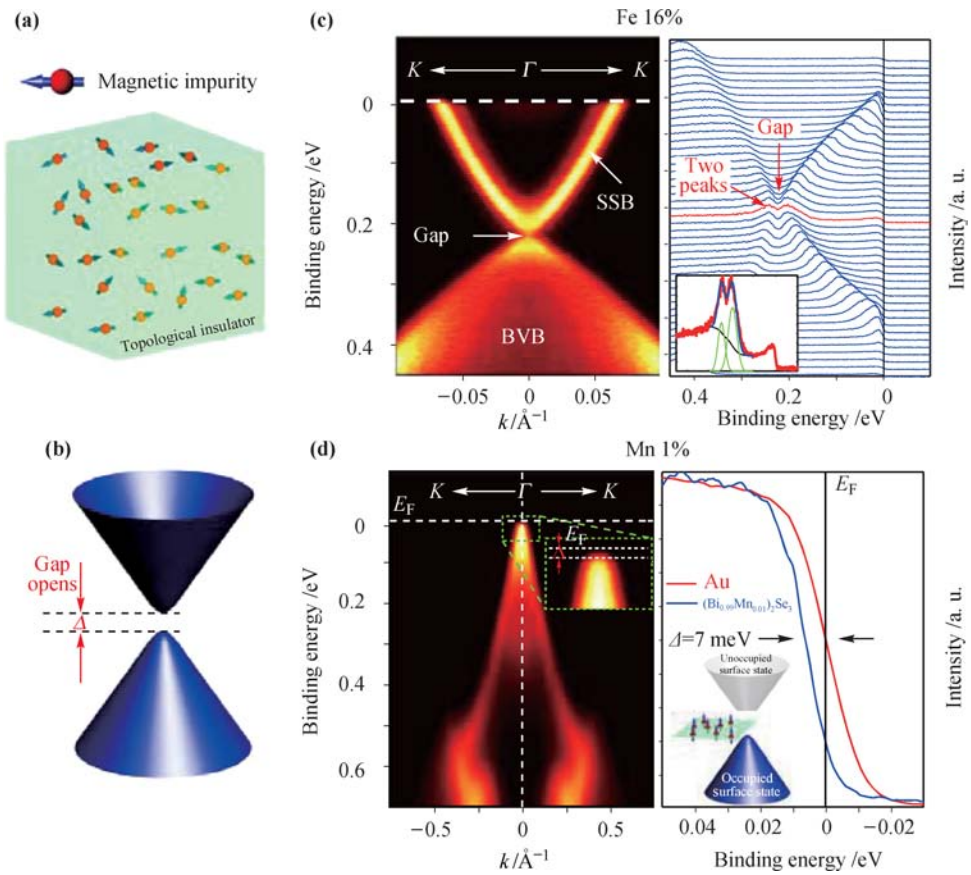


**Fig. 19** **(a, b)** A magnetically doped topological insulator with a broken Dirac point and a gap separating the upper and lower Dirac cones. **(c)** Band structure of an Fe-doped samples with melt composition $(Bi_{0.84}Fe_{0.16})_2Se_{3.7}$. At the Dirac point, the reduced spectral intensity (left subpanels) and the twin-peak structure in the EDCs (right subpanels) indicate a gap formation. **(d)** Left panel: ARPES spectra intensity plot along the $K$–$\Gamma$–$K$ direction of Mn-doped $(Bi_{0.99}Mn_{0.01})_2Se_3$ showing the $E_F$ inside the surface Dirac gap. Inset: close-up of the dispersion in the vicinity of $E_F$, indicating a gap between the leading edge of the SSB and $E_F$. Vertical white dashed line shows the location of the EDC plotted in the right panel. Right panel: Comparison between the $\Gamma$ point EDC (*blue*) and $E_F$ shows a leading-edge gap of 7 meV. A reference EDC from a polycrystalline Au sample whose leading edge, as expected, coincides with $E_F$ is shown in red. Inset shows the illustration of the insulating massive Dirac fermion state. Reproduced from Ref. [25], Copyright © 2010 American Association for the Advancement of Science.

combine the magnetic and charge doping together to achieve this. For example, it is possible to introduce much Fe dopants into $Bi_2Se_3$ to increase the gap size without substantially altering the $E_F$ position relative to the undoped $Bi_2Se_3$; then we can move $E_F$ into the gap by introducing additional p-type dopants such as Magnesium [25]. We can achieve a larger gap while preserving the insulating nature of the state.

Besides the example above, the unique robustness of the surface state of TIs and the effect of broken TRS by another study can be seen in Ref. [58].

### 3.4 Search for other TI materials

Despite the exciting progress made in the last couple of years, the field of TIs is still in its early development. Many of the amazing topological effects and their potential applications are still limited by the non-ideal properties of current TI materials.

For example, to date, the 2D quantum spin Hall effect was discovered only in the HgTe/CdTe quantum well system, and the small gap (∼20 meV) of HgTe/CdTe quantum well prevents it from being used for high (room) temperature applications. In the 3D case, while the $Bi_2Te_3/Bi_2Se_3$ family of materials have the bulk gap up to 200 meV, the layered nature and the van der Waals force bonding between quintuple layers makes it difficult to shape into the desired forms for transport measurement and applications; and foreign atoms can be easily adsorbed on the surface (see Fig. 20 for the aging curve of a pristine $Bi_2Se_3$ in the UHV environments) and even get into the interstitial space between quintuple layers [59], introducing undesired impurities and charge dopings [16, 25, 60]. These problems thus provide the motivation for the search for more TI materials with better chemical, physical and electronic properties.

In Fig. 21, we give an example to illustrate the recent discovery of a new TI family in III–V–$VI_2$ compounds [28]. From panels (a)–(d), the characteristic single Dirac cone at the $\Gamma$ point immediately discoveres the

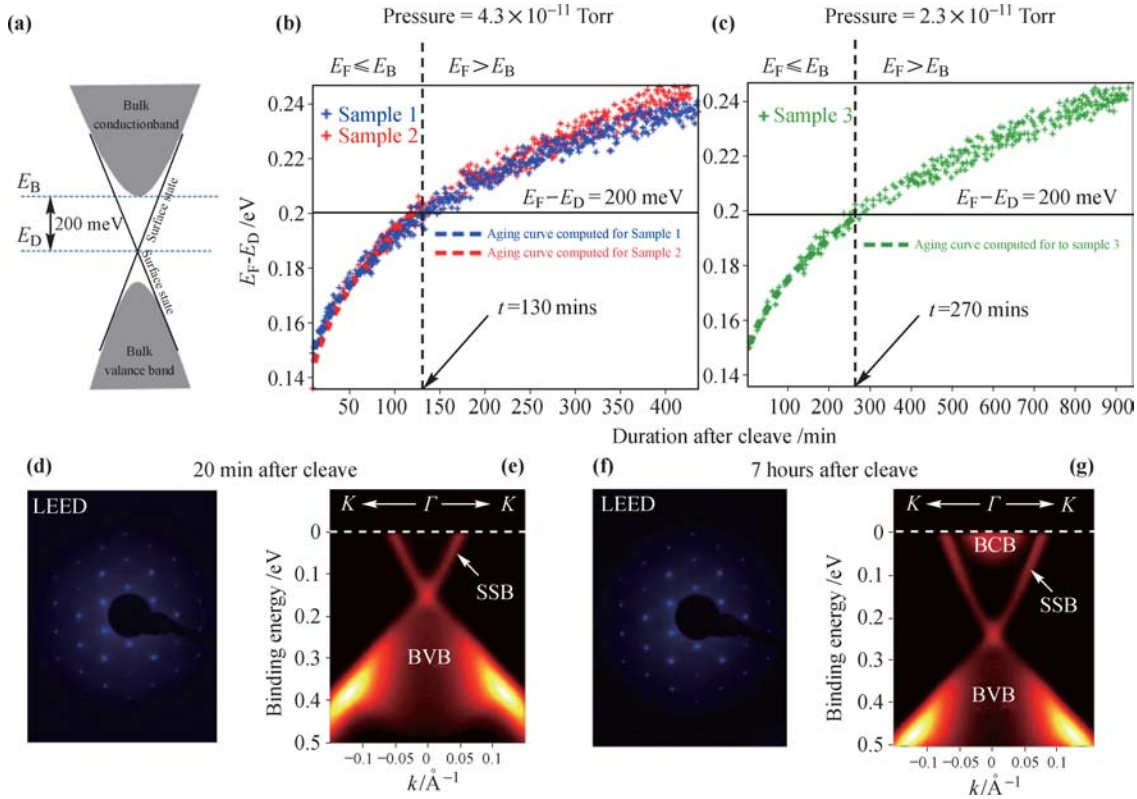


**Fig. 20** Time dependent band structure study on samples with initial $E_F$ inside the bulk gap. **(a)** Simple illustration of the band structure of $Bi_2Se_3$ **(b, c)** Evolution of $E_F - E_D$ value of three samples (with the growth melt composition $Bi_{1.7}Se_{3.3}$) with time measured at different chamber pressures. For the pressure $p = 4.3 \times 10^{-11}$ Torr, it took ∼130 minutes for $E_F$ of both measured samples to reach the bottom of BCB ($E_F - E_D \approx 200$ meV, see b), while for the better pressure case $p = 2.3 \times 10^{-11}$ Torr, it took about twice as long (∼270 mins) for $E_F$ to reach the same position (see c). Cyan/yellow/green dashed lines show the calculated aging curves (see text) that agree well with the measurements. **(d)–(g)** Low energy electron diffraction (LEED) measurements (d, f) and ARPES measurements on the band structure (e, g) performed at 20 minutes and 7 hours after a freshly cleaved surface. The LEED pattern is identical while the $E_F$ of the band structure up-shifts by ∼100 meV. Reproduced from Ref. [25], Copyright © 2010 American Association for the Advancement of Science.

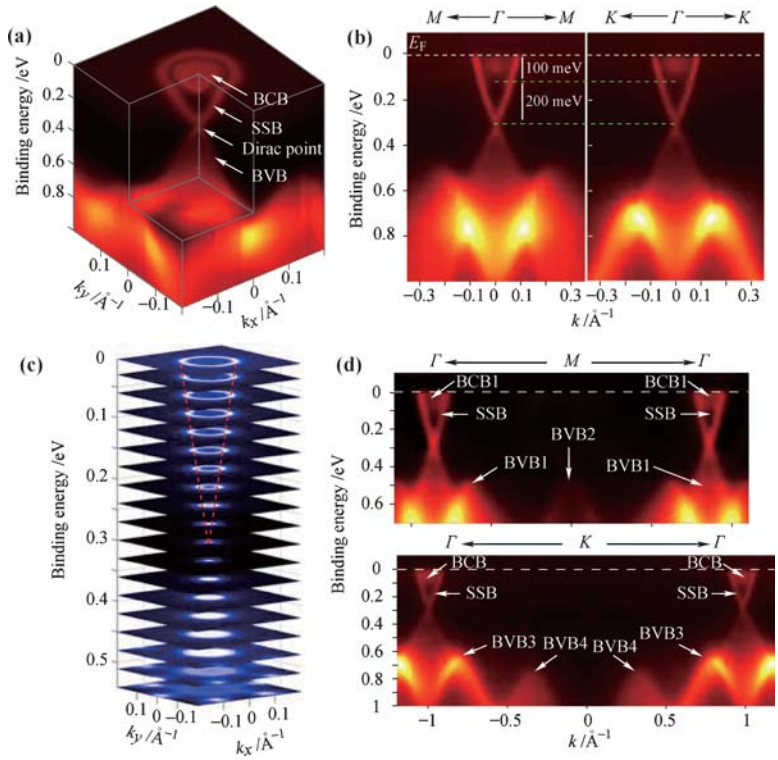


**Fig. 21** **(a)** Dispersions of n-doped TI $TlBiSe_2$ along two high symmetry directions, indicating a bulk gap of ∼ 200 meV and a single surface Dirac fermion around the $\Gamma$ point. **(b)** 3D band structure of $TlBiTe_2$ around $\Gamma$, with the BCB, BVB, SSB and the Dirac point labeled. **(c)** Dispersion along $M$–$\Gamma$–$K$ direction. Four regions defined by characteristic energy positions are labeled as I, II, III, and IV, respectively. **(d)** Four constant energy plots of the band structure from region-III defined in (c), showing the six characteristic BVB hole pockets outside the SSB pocket, as demonstrated in the cartoon on the bottom row. Reproduced from Ref. [28], Copyright © 2010 American Physical Society.

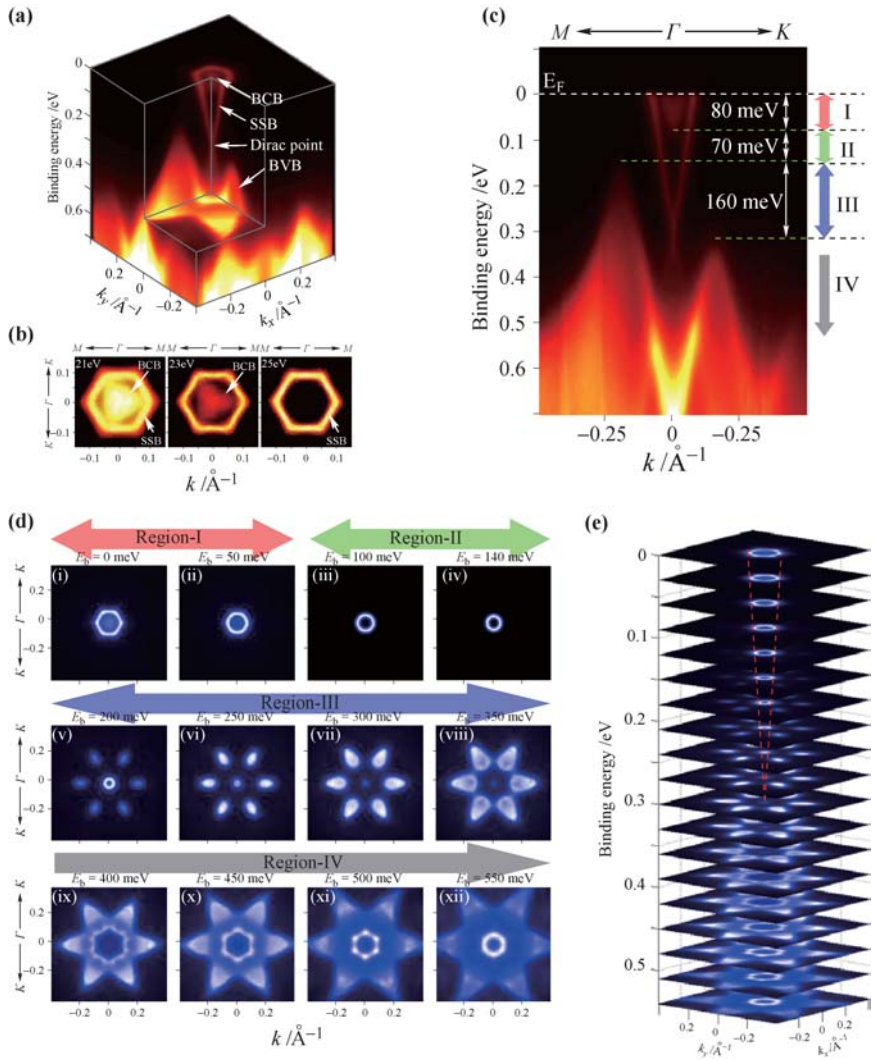


**Fig. 22** **(a)** Dispersions of n-doped TI $TlBiSe_2$ along two high symmetry directions, indicating a bulk gap of $\sim$ 200 meV and a single surface Dirac fermion around the $\Gamma$ point. **(b)** 3D band structure of $TlBiTe_2$ around $\Gamma$, with the BCB, BVB, SSB and the Dirac point labeled. **(c)** Dispersion along $M$–$\Gamma$–$K$ direction. Four regions defined by characteristic energy positions are labeled as I, II, III, and IV, respectively. **(d)** Four constant energy plots of the band structure from region-III defined in (c), showing the six characteristic BVB hole pockets outside the SSB pocket, as demonstrated in the cartoon on the bottom row. Reproduced from Ref. [28], Copyright © 2010 American Physical Society.

topological nontrivial nature of this compound, and a bulk gap of $\sim$ 200 meV in $TlBiSe_2$ is shown in Fig. 21(b), similar to that of $Bi_2Se_3$. However, compared to the $Bi_2Se_3$ family of compounds, this new family has much better physical properties due to the covalence bonding between atomic layers in $TlBiSe_2$, which is much stronger [27, 31] than the van de Waals force that bonds quintuple layer units of $Bi_2Te_3$ or $Bi_2Se_3$ [13]. This makes this material much more favorable for other measurements and applications.

Besides the single surface Dirac fermion, materials in the III–V–$VI_2$ family can also possess other interesting properties. One such example is shown in Fig. 22, where the band structure of another compound, $TlBiTe_2$, is summarized. Besides having the Dirac surface state, $TlBiTe_2$ was reported to show a bulk superconducting transition at $T = 0.14$ K when p-doped to the carrier density $6 \times 10^{20}/\text{cm}^3$ [61]. At this doping level, the $E_F$ of the system is $\sim$ 150 meV below the BCB bottom and resides in a region [see region III in Fig. 22(c)] where the FS geometry is characterized by a ringlike SSB FS and six surrounding p-type bulk pockets [Fig. 22(d)].

As the six leaf-like bulk pockets are the only bulk electronic features at this doping [see Fig. 23(a), (b)], it naturally indicates that they are the origin of the the bulk superconductivity of p-type $TlBiTe_2$. Furthermore, in the superconducting state, the surface state can also become superconducting due to the proximity effect. For such a superconductor, it has been proposed [23] that each vortex line has two Majorana zero modes related by the time reversal symmetry, making it a candidate for the long sought topological superconductors (which will be discussed below) and for the topological quantum computation [62].

Interestingly, the ternary III–V–$VI_2$ family compounds are also known as good high-temperature thermoelectric materials [63–68], and a long standing puzzle since 1960s has been the unusually low thermoelectric figure of merit ($ZT$) of $TlBiTe_2$ ($ZT \sim 0.15$) due to its much smaller thermoelectric power $S$ ($\sim$ 70 μV/K) [63, 65] compared to that of other compounds ($ZT \sim 0.9, S \sim$ 200 μV/K) [66, 67] in the family. By observing a negative

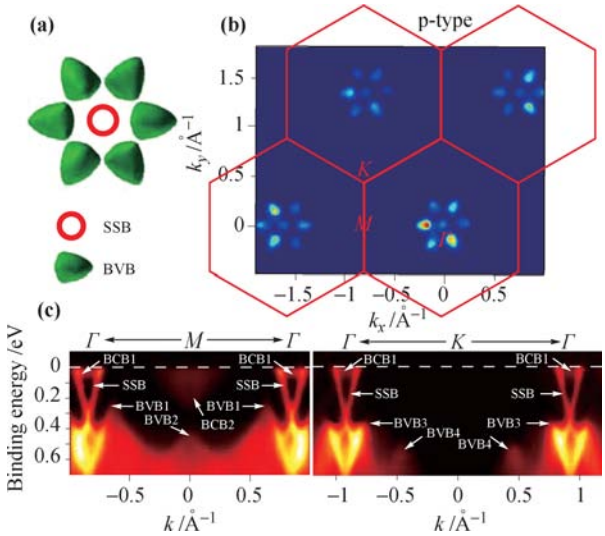


**Fig. 23** Typical FS geometry in region III as defined in Fig. 22. **(b)** Broad $k$-space scan shows no additional features besides the FS pockets illustrated in (a). High symmetry points $\Gamma$, $M$, and $K$ are marked; the uneven intensity at different BZs results from the matrix element effect. **(c)** Broad $k$-space experimental band structures, with the prominent BCB, BVB, and SSB features labeled. There is a small energy overlap ($\sim$ 20 meV) between the BVB1 and BCB2 in the $\Gamma$–$M$–$\Gamma$ direction scan. Reproduced from Ref. [28], Copyright © 2010 American Physical Society.

band gap in the band structure [Fig. 23(c)], we demonstrate that $TlBiTe_2$ is a semi-metal, in contrast to a narrow-gap semiconductor as conventionally believed [64, 68], and naturally explains its mysteriously small thermoelectric power [28]. The opposite contributions of the simultaneous existing electron and hole pockets greatly reduce the total thermoelectric power $S$, which leads to further suppress of its thermoelectric figure of merit as $ZT = S^2\sigma/(\kappa T)$.

Besides the III–V–$VI_2$ compounds shown above, there are also other TIs proposed, such as the many half heusler materials [32, 33]. In addition, surprises keep coming from the exiting family of materials such as the dramatic reduction of residual bulk carrier density in the variation of $V_2$–$VI_3$ TI materials [69, 70] and the Dirac surface state arising from the bulk HgTe (Fig. 24 [71]). Furthermore, besides the TIs in weakly interacting systems, TIs from strongly correlated materials are also actively investigated [39, 40]. The study of TIs in these materials will not only extend our understanding on topological properties of future TI materials, but also help us improve the materials' properties of future TIs (e.g., more insulating and larger gap) for practical applications.

### 3.5 Other topological states and perspectives

Following the discovery in 2D and 3D materials, TIs have grown as one of the most intensively studied fields in condensed matter physics. The swift development of TIs also inspires the study of other topological states, such as

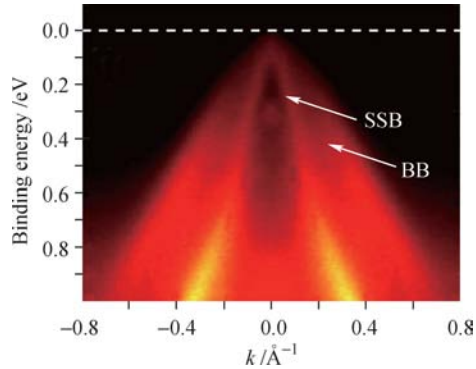


**Fig. 24** ARPES measurements on a relaxed, 1-μm-thick HgTe sample. The dispersion of the surface state (SSB) and bulk bands (BB) are indicated by the arrows. Reproduced from Ref. [71], Copyright © 2011 American Physical Society.

quantum anomalous Hall insulators [72] and topological superconductors [19].

In a quantum anomalous Hall insulator, spontaneous magnetic moments and spin–orbit coupling combine to build a topologically nontrivial electronic structure, leading to the quantized Hall effect without an external magnetic field. The quantum anomalous Hall effect is the last quantized effect in the Hall effect family besides the Hall effect and the spin Hall effect. Given the large separation between the conducting channels, the back scattering of the electron can be suppressed even in the presence of magnetic impurities, signaling promising low power applications.

A topological superconductor has a pairing gap in the bulk and topologically protected surface state consisting of Majorana fermions [23]. Unlike Dirac fermions in TIs that can have the form of particles or holes, Majorana fermions are their own antiparticles [23, 26, 73–75]. The simplest 3D topological superconductor consists of a single Majorana cone on the surface, containing half the degree of freedom of the Dirac surface state for a single cone 3D TI. This fractionalization of the degree of freedom introduces quantum non-locality and is essential for the topological quantum computing based on Majorana fermions [62].

The study of these new quantum materials will not only be of great scientific interests, but also provide new opportunities for novel applications. We believe that the ARPES technique will continue to be an important tool in the research on novel topological quantum materials, and greatly contribute to the development in this new frontier.

**Acknowledgements** We would like to express our gratitude to our colleagues at Stanford for their cooperation, daily discussion and many useful comments: Zhi-Xun Shen, Shoucheng Zhang, Ian R. Fisher, Xiaoliang Qi, Aharon Kapitulnik, James G. Analytis, Zhongkai Liu, Haijun Zhang, Jiun-Haw Chu, Donghui Lu, Rob G. Moore, Yi Cui, and Desheng Kong. We would also like to take this opportunity to acknowledge our collaborators in the field: Zahid Hussain, Takao Sasagawa, Laurens Molenkamp, Zhong Fang, Xi Dai, Sung-Kwan Mo, Binghai Yan, Chaoxing Liu and Hailin Peng.

This work was supported by DARPA award DARPA-BAA-11-07.

## References


1. P. Anderson, Basic Notions of Condensed Matter Physics, Reading: Addison-Wesley, 1997
2. K. v. Klitzing, G. Dorda, and M. Pepper, Phys. Rev. Lett., 1980, 45: 494
3. D. J. Thouless, M. Kohmoto, M. P. Nightingale, and M. den Nijs, Phys. Rev. Lett., 1982, 49: 405
4. J. Bellissard, A. van Elst, and H. Schulz-Baldes, J. Math. Phys., 1994, 35: 5373
5. X. L. Qi and S. C. Zhang, Phys. Today, 2010, 63: 33
6. L. Fu and C. L. Kane, Phys. Rev. B, 2007, 76: 045302
7. X. L. Qi, T. L. Hughes, and S. C. Zhang, Phys. Rev. B, 2008, 78: 195424
8. C. L. Kane and E. J. Mele, Phys. Rev. Lett., 2005, 95: 226801
9. C. L. Kane and E. J. Mele, Phys. Rev. Lett., 2005, 95: 146802
10. B. A. Bernevig, T. L. Hughes, and S. C. Zhang, Science, 2006, 314: 1757
11. M. König, S. Wiedmann, C. Brüne, A. Roth, H. Buhmann, L. W. Molenkamp, X. L. Qi, and S. C. Zhang, Science, 2007, 318: 766
12. D. Hsieh, D. Qian, L. Wray, Y. Xia, Y. S. Hor, R. J. Cava, and M. Z. Hasan, Nature, 2008, 452: 970
13. H. Zhang, C. Liu, X. Qi, X. Dai, Z. Fang, and S. Zhang, Nat. Phys., 2009, 5: 438
14. Y. Xia, D. Qian, D. Hsieh, L. Wray, A. Pal, H. Lin, A. Bansil, D. Grauer, Y. Hor, R. Cava, and M. Z. Hasan, Nat. Phys., 2009, 5: 398
15. D. Hsieh, Y. Xia, D. Qian, L. Wray, J. H. Dil, F. Meier, J. Osterwalder, L. Patthey, J. G. Checkelsky, N. P. Ong, A. V. Fedorov, H. Lin, A. Bansil, D. Grauer, Y. S. Hor, R. J. Cava, and M. Z. Hasan, Nature, 2009, 460: 1101
16. Y. L. Chen, J. G. Analytis, J. H. Chu, Z. K. Liu, S. K. Mo, X. L. Qi, H. J. Zhang, D. H. Lu, X. Dai, Z. Fang, S. C. Zhang, I. R. Fisher, Z. Hussain, and Z. X. Shen, Science, 2009, 325: 178
17. P. Roushan, J. Seo, C. V. Parker, Y. S. Hor, D. Hsieh, D. Qian, A. Richardella, M. Z. Hasan, R. J. Cava, and A. Yazdani, Nature, 2009, 460: 1106
18. L. Fu, C. L. Kane, and E. J. Mele, Phys. Rev. Lett., 2007, 98: 106803
19. L. Fu, Phys. Rev. Lett., 2009, 103: 266801
20. A. R. Akhmerov, J. Nilsson, and C. W. J. Beenakker, Phys. Rev. Lett., 2009, 102: 216404
21. J. E. Moore and L. Balents, Phys. Rev. B, 2007, 75: 121306
22. R. Roy, Phys. Rev. B, 2009, 79: 195321
23. X. L. Qi, T. L. Hughes, S. Raghu, and S. C. Zhang, Phys. Rev. Lett., 2009, 102: 187001
24. L. Fu and E. Berg, Phys. Rev. Lett., 2010, 105: 097001
25. Y. L. Chen, J. H. Chu, J. G. Analytis, Z. K. Liu, K. Igarashi, H. H. Kuo, X. L. Qi, S. K. Mo, R. G. Moore, D. H. Lu, M. Hashimoto, T. Sasagawa, S. C. Zhang, I. R. Fisher, Z. Hussain, and Z. X. Shen, Science, 2010, 329: 659
26. Y. Hor, J. Checkelsky, D. Qu, N. Ong, and R. Cava, J. Phys. Chem. Solids, 2011, 72: 572
27. B. Yan, C. X. Liu, H. J. Zhang, C. Y. Yam, X. L. Qi, T. Frauenheim, and S. C. Zhang, Europhys. Lett., 2010, 90: 37002
28. Y. L. Chen, Z. K. Liu, J. G. Analytis, J. H. Chu, H. J. Zhang, B. H. Yan, S. K. Mo, R. G. Moore, D. H. Lu, I. R. Fisher, S. C. Zhang, Z. Hussain, and Z. X. Shen, Phys. Rev. Lett., 2010, 105: 266401
29. H. Min, J. E. Hill, N. A. Sinitsyn, B. R. Sahu, L. Kleinman, and A. H. MacDonald, Phys. Rev. B, 2006, 74: 165310
30. Y. Yao, F. Ye, X. L. Qi, S. C. Zhang, and Z. Fang, Phys. Rev. B, 2007, 75: 041401
31. H. Lin, R. S. Markiewicz, L. A. Wray, L. Fu, M. Z. Hasan, and A. Bansil, Phys. Rev. Lett., 2010, 105: 036404
32. S. Chadov, X. Qi, J. Kübler, G. H. Fecher, C. Felser, and S. C. Zhang, Nat. Mater., 2010, 9: 541
33. H. Lin, L. Wray, Y. Xia, S. Xu, S. Jia, R. Cava, A. Bansil, and M. Hasan, Nat. Mater., 2010, 9: 546
34. M. P. Seah and W. A. Dench, Surface and Interface Analysis, 1979, 1: 2, http://dx.doi.org/10.1002/sia.740010103
35. A. Becquerel, CR (East Lansing, Mich.), 1839, 9: 561
36. H. Hertz, Annalen der Physik, 1887, 267: 421
37. A. Einstein, Ann. Phys., 1906, 20: 199
38. B. Feuerbacher, B. Fitton, and R. Willis, Photoemission and The Electronic Properties of Surfaces, New York (London): Wiley, 1978
39. A. Shitade, H. Katsura, J. Kunes, X. L. Qi, S. C. Zhang, and N. Nagaosa, Phys. Rev. Lett., 2009, 102: 256403
40. X. Wan, A. M. Turner, A. Vishwanath, and S. Y. Savrasov, Phys. Rev. B, 2011, 83: 205101
41. W. Röentgen, Sitzungsberichte der Physikalisch–Medizischen Gesellschaft in Wurzburg, Phys. Medi. Society, 1895, S. 132–141, Band 137
42. A. J. Nicholson, Appl. Opt., 1970, 9: 1155
43. F. Elder, A. Gurewitsch, R. Langmuir, and H. Pollock, Phys. Rev., 1947, 71: 829
44. T. H. Maiman, Nature, 1960, 187: 493
45. A. Lienard, L' Eclairage Elec., 1898, 16: 5
46. D. H. Bilderback, P. Elleaume, and E. Weckert, J. Phys. B, 2005, 38: S773
47. E. Fermi, Zeits. f. Physik, 1934, 88: 172
48. D. Hsieh, Y. Xia, L. Wray, D. Qian, A. Pal, J. H. Dil, J. Osterwalder, F. Meier, G. Bihlmayer, C. L. Kane, Y. S. Hor, R. J. Cava, and M. Z. Hasan, Science, 2009, 323: 919
49. D. Hsieh, Y. Xia, D. Qian, L. Wray, F. Meier, J. H. Dil, J. Osterwalder, L. Patthey, A. V. Fedorov, H. Lin, A. Bansil, D. Grauer, Y. S. Hor, R. J. Cava, and M. Z. Hasan, Phys. Rev. Lett., 2009, 103: 146401
50. Z. Alpichshev, J. Analytis, J. Chu, I. Fisher, Y. Chen, Z. Shen, A. Fang, and A. Kapitulnik, Phys. Rev. Lett., 2010, 104: 16401
51. S. Souma, K. Kosaka, T. Sato, M. Komatsu, A. Takayama, T. Takahashi, M. Kriener, K. Segawa, and Y. Ando, Phys. Rev. Lett., 2011, 106: 216803
52. S.-Y. Xu, L. A. Wray, Y. Xia, F. von Rohr, Y. S. Hor, J. H. Dil, F. Meier, B. Slomski, J. Osterwalder, M. Neupane, H. Lin, A. Bansil, A. Fedorov, R. J. Cava, and M. Z. Hasan, arXiv: 1101.3985v1, 2011
53. Y. Zhang, K. He, C. Z. Chang, C. L. Song, L. L. Wang, X. Chen, J. F. Jia, Z. Fang, X. Dai, W. Y. Shan, S.-Q. Shen, Q. Niu, X.-L. Qi, S.-C. Zhang, X.-C. Ma, and Q.-K. Xue, Nat. Phys., 2010, 6: 584

54. C. X. Liu, H. Zhang, B. Yan, X. L. Qi, T. Frauenheim, X. Dai, Z. Fang, and S. C. Zhang, Phys. Rev. B, 2010, 81: 041307
55. X. L. Qi, R. Li, J. Zang, and S. C. Zhang, Science, 2009, 323: 1184
56. J. Zang and N. Nagaosa, Phys. Rev. B, 2010, 81: 245125
57. F. Wilczek, Nature, 2009, 458: 129
58. L. A. Wray, S.Y. Xu, Y. Xia, D. Hsieh, A. V. Fedorov, Y. S. Hor, R. J. Cava, A. Bansil, H. Lin, and M. Z. Hasan, Nat. Phys., 2011, 7: 32
59. G. Wang, X. G. Zhu, Y. Y. Sun, Y. Y. Li, T. Zhang, J. Wen, X. Chen, K. He, L. L. Wang, X. C. Ma, J. F. Jia, S. B. Zhang, and Q. K. Xue, Adv. Mater., 2011, 23: 2929, http://dx.doi.org/10.1002/adma.201100678
60. J. G. Analytis, J. H. Chu, Y. Chen, F. Corredor, R. D. McDonald, Z. X. Shen, and I. R. Fisher, Phys. Rev. B, 2010, 81: 205407
61. R. A. Hein and E. M. Swiggard, Phys. Rev. Lett., 1970, 24: 53
62. C. Nayak, S. H. Simon, A. Stern, M. Freedman, and S. Das Sarma, Rev. Mod. Phys., 2008, 80: 1083
63. D. P. Spitzer and J. A. Sykes, J. Appl. Phys., 1966, 37: 1563
64. K. Chrissafis, E. S. Vinga, K. M. Paraskevopoulos, and E. K. Polychroniadis, Physica Status Solidi (a), 2003, 196: 515
65. K. Kurosaki, A. Kosuga, and S. Yamanaka, J. Alloys Comp., 2003, 351: 279
66. K. Kurosaki, H. Uneda, H. Muta, and S. Yamanaka, J. Alloys Comp., 2004, 376: 43
67. K. F. Hsu, S. Loo, F. Guo, W. Chen, J. S. Dyck, C. Uher, T. Hogan, E. K. Polychroniadis, and M. G. Kanatzidis, Science, 2004, 303: 818
68. K. Hoang and S. D. Mahanti, Phys. Rev. B, 2008, 77: 205107
69. J. Analytis, R. McDonald, S. Riggs, J. Chu, G. Boebinger, and I. Fisher, Nat. Phys., 2010, 6: 960
70. Z. Ren, A. A. Taskin, S. Sasaki, K. Segawa, and Y. Ando, Phys. Rev. B, 2010, 82: 241306
71. C. Brüne, C. X. Liu, E. G. Novik, E. M. Hankiewicz, H. Buhmann, Y. L. Chen, X. L. Qi, Z. X. Shen, S. C. Zhang, and L. W. Molenkamp, Phys. Rev. Lett., 2011, 106: 126803
72. R. Yu, W. Zhang, H. J. Zhang, S. C. Zhang, X. Dai, and Z. Fang, Science, 2010, 329: 61
73. F. Wilczek, Nat. Phys., 2009, 5: 614
74. X. L. Qi, T. L. Hughes, and S. C. Zhang, Phys. Rev. B, 2010, 81: 134508
75. A. P. Schnyder, S. Ryu, A. Furusaki, and A. W. W. Ludwig, Phys. Rev. B, 2008, 78: 195125
76. A. Nishide, A. A. Taskin, Y. Takeichi, T. Okuda, A. Kakizaki, T. Hirahara, K. Nakatsuji, F. Komori, Y. Ando, and I. Matsuda, Phys. Rev. B, 2010, 81: 041309(R)
77. Y. Y. Li, G. Wang, X. G. Zhu, M. H. Liu, C. Ye, X. Chen, Y. Y. Wang, K. He, L. L. Wang, X. C. Ma, H. J. Zhang, X. Dai, Z. Fang, X. C. Xie, Y. Liu, X. L. Qi, J. F. Jia, S. C. Zhang, and Q. K. Xue, Adv. Mater., 2010, 22: 4002